processes

MDPI

Article

Experimental Evaluation of Blockage Resistance and Position Caused by Microparticle Migration in Water Injection Wells

Jifei Yu [1,2,†], Huan Chen [1,2,†], Yanfeng Cao [1,2,†], Min Wen [1,2], Xiaopeng Zhai [3,*], Xiaotong Zhang [1,2], Tongchuan Hao [1,2], Jianlin Peng [1,2] and Weitao Zhu [1,2]

[1] State Key Laboratory of Offshore Oil and Gas Exploitation, Beijing 100020, China; yujf2@cnooc.com.cn (J.Y.); chenhuan3@cnooc.com.cn (H.C.); caoyf@cnooc.com.cn (Y.C.); wenmin@cnooc.com.cn (M.W.); zhangxt37@cnooc.com.cn (X.Z.); haotch@cnooc.com.cn (T.H.); pengjl7@cnooc.com.cn (J.P.); zhuwt3@cnooc.com.cn (W.Z.)
[2] CNOOC Research Institute Co., Ltd., Beijing 100028, China
[3] Hubei Key Laboratory of Oil and Gas Drilling and Production Engineering, Yangtze University, Wuhan 430100, China
* Correspondence: zhaixp@yangtzeu.edu.cn
† These authors contributed equally to this work.

Abstract: Offshore oil field loose sandstone reservoirs have high permeability. However, during the water injection process, water injection blockage occurs, causing an increase in injection pressure, making it impossible to continue injecting water on site. Current research mainly focuses on the factors causing water injection blockage, with less attention given to the blockage locations and the pressure increase caused by water injection. There is a lack of research on the change in the law of injection capacity. This paper establishes a simulation experiment for water injection blockage that can accommodate both homogeneous and heterogeneous cores. The experimental core is 1 m long and capable of simulating the blockage conditions in the near-well zone during water injection, thereby analyzing the core blockage position and blockage pressure. The study clarifies the influence of water quality indicators, heterogeneity, and core length on the blockage patterns in reservoirs during water injection. The research findings are as follows: I. The reservoir blockage samples were characterized using scanning electron microscopy (SEM), casting thin sections, and X-ray diffraction (XRD) analysis. The results indicate that the main factors causing blockage are clay, silt, and fine particulate suspensions, with the fine particles mainly consisting of hydrated silicates and alkali metal oxides. The primary cause of blockage in loose sandstone is identified as the mechanism of migration and accumulation of clay, fine rock particles, and suspended matter in the injected water. II. By monitoring pressure and permeability changes in the core flooding experiments, the impact of reservoir heterogeneity on water injection capacity was evaluated. The evaluation results show that the blockage locations and lengths in heterogeneous cores are twice those in homogeneous cores. III. For heterogeneous reservoirs, if the initial permeability at the inlet is lower than in other segments of the core, significant blockage resistance occurs, with the final resistance being 1.27 times that of homogeneous cores. If the initial permeability at the inlet is higher than in other parts, the final blockage resistance is close to that of homogeneous cores. This study provides theoretical support for the analysis of blockage locations and pressures in loose sandstone water injection and offers technical support for the design of unplugging ranges and pressures after blockage in heterogeneous formations. At the same time, it provides a theoretical basis for selecting the direction of acidizing after blockage occurs in loose sandstone.

Keywords: water injection; blockage; blockage pressure; heterogeneity; particle migration

Citation: Yu, J.; Chen, H.; Cao, Y.; Wen, M.; Zhai, X.; Zhang, X.; Hao, T.; Peng, J.; Zhu, W. Experimental Evaluation of Blockage Resistance and Position Caused by Microparticle Migration in Water Injection Wells. *Processes* **2024**, *12*, 2275. https://doi.org/10.3390/pr12102275

Academic Editor: Václav Uruba

Received: 12 September 2024
Revised: 12 October 2024
Accepted: 14 October 2024
Published: 17 October 2024

1. Introduction

To increase production, loose sandstone reservoirs require a large amount of water injection during the production process to achieve the desired production enhancement.

However, after multiple rounds of water injection, the injection pressure increases, reaching the injection pressure limit at the wellhead, making it difficult to further increase the pressure or the injection volume [1–3]. For example, the Guantao Formation sandstone reservoir in the C Oilfield of the Bohai Sea area is mainly a bottom-water reservoir with a strong edge and bottom-water drive. It has a porosity between 28% and 34%, with an average porosity of 29.3%, and permeability between 100 and 3000 mD, with an average permeability of 1600 mD, exhibiting high porosity and high permeability reservoir characteristics [4–6]. The reservoir space is primarily composed of primary pores with good pore connectivity; the pore throat radius ranges from 0.055 to 26.3 μm, with an average pore throat radius of 7.5 μm. Water injection officially began in March 2017, with an initial injection pressure of around 5 MPa, but the injection volume was less than 100 m^3/d. Subsequently, the wellhead pressure quickly rose to 10 MPa, reaching the injection pressure limit, making it impossible to continue increasing the injection volume [7–9].

This phenomenon is relatively common in the water injection process of loose sandstone reservoirs [10,11]. Currently, it is generally believed that the cause of this phenomenon is that the pore throats of the reservoir become blocked during water injection, leading to an increase in injection pressure and making it difficult to continue injecting.

Therefore, more research has focused on the causes of water injection blockage, such as particle capture and deposition, which primarily refers to the migration and blockage of reservoir microparticles in pore throats due to changes in fluid contact conditions [12,13]. The mechanism of microparticle and suspended matter blockage refers to the deposition and aggregation of small particles and suspended matter during fluid flow in oil and gas field development [14,15]. This leads to obstruction of the pore structure and a resulting decline in permeability.

The particle bridging effect and the intrusion of external solid phases occur when solid particles from various operational fluids invade the reservoir along with the working fluids, causing damage by depositing in the pore throats of the reservoir. Microparticles form bridging structures within the pore throats, where particles interact and create bridges in the pores. During fluid flow, microparticles and suspended matter can be captured or deposited at the pore throats [16,17]. This capture and deposition gradually increase resistance, obstructing fluid flow, narrowing fluid pathways, and ultimately causing a decrease in permeability.

However, most of the current research on water injection blockage focuses on the macro perspective, studying how different factors affect reservoir permeability after blockage during the water injection process [18,19].

Macro studies suggest that permeability damage in water injection wells primarily comes from two aspects. Firstly, damage caused by the invasion of working fluids into the reservoir, which leads to clay swelling, water blocking, and fluid incompatibility. For instance, Mitra A et al. determined through linear expansion rate experiments with clay content that the invasion of drilling fluids causes rock expansion, thereby reducing reservoir permeability [20]. Yang et al. argued that if the injected water is incompatible with the reservoir fluids, chemical reactions may occur, generating insoluble inorganic scales like calcium salts, magnesium salts, barium salts, and iron salts, which could accumulate in rock pores and fractures, leading to reduced permeability in coal rock and damage to the reservoir [21]. Liu et al. stated that core blockage depends on variables such as the mineral composition of the reservoir, pressure, injection rate, injected fluid composition, and pH value. Differential pressure, water sensitivity damage, and drilling fluid compatibility are considered the main factors causing blockage and damage to the reservoir [22]. Secondly, the stress-sensitivity damage of coal reservoirs. Yao et al. found that coal cores exhibit strong stress sensitivity, and as the contamination pressure increases, the permeability recovery value of the reservoir core decreases sharply [23]. Yang et al. tested that after water injection, the stress sensitivity coefficient of the core increased from 0.73 to 0.79, indicating that water injection further enhances the stress sensitivity of the reservoir [24].

Cheraghian et al. suggested that water injection blockage is related to the solid phase in the water, water sensitivity of the reservoir, and pressure sensitivity [25].

Microparticles migrating in rock pores and fractures are influenced by various factors [26,27]. In recent years, scholars have conducted extensive theoretical and experimental research to study the migration patterns of microparticles in these fractures. Based on a self-developed experimental device for evaluating microparticle migration and sedimentation, different fluid conditions (fluid salinity and flow rate) were set up for displacing experiments [28]. The research found that microparticle migration and blockage in the near-well fractures are significant factors contributing to blockage, with microparticles severely damaging permeability and flow capacity, and the damage degree increasing sharply with higher microparticle concentrations [29,30]. However, the process of microparticle migration causing blockage in reservoirs remains a "black box", and the suspension and sedimentation patterns of microparticles in the pores are still unknown.

Although a considerable amount of research has been performed on permeability after water injection blockage, determining the blockage pressure and blockage location after blockage remains the key to solving the blockage problem [31,32]. However, current laboratory experiments use core samples that are too short, usually 5–10 mm, making it impossible to analyze blockage pressure and blockage location after water injection [33,34]. This also results in a lack of evaluation of water injection capacity and studies on the patterns of its variation.

Therefore, this paper establishes a simulation experiment for water injection blockage that can accommodate both homogeneous and heterogeneous cores. The experimental core is 1 m long and capable of simulating the blockage conditions in the near-well zone during water injection. The research aims to explore the influence of core heterogeneity and driving flow rate on the permeability of coal samples when water is injected, to determine the changes in blockage location and pressure caused by water injection blockage, and to guide future work in removing blockages during water injection.

2. Materials and Methods

2.1. Mechanism of Fine Particles and Suspended Solids Blockage

Offshore loose sandstone reservoirs have high permeability and a high clay mineral content, typically exceeding 10%. The clay minerals are primarily argillaceous cement, with illite and mixed-layer illite–smectite being dominant. During water injection, the high content of clay minerals, such as illite and kaolinite, leads to a significant velocity sensitivity effect. The grain size in loose sandstone reservoirs mainly ranges from 0.05 mm to 1 mm, with a large surface area that makes them prone to dispersion, as shown in Figure 1a. Some clays with strong water sensitivity are highly susceptible to hydration and swelling, and they mix with organic particles, iron corrosion products, and formation fines to form suspended solids, as shown in Figure 1b.

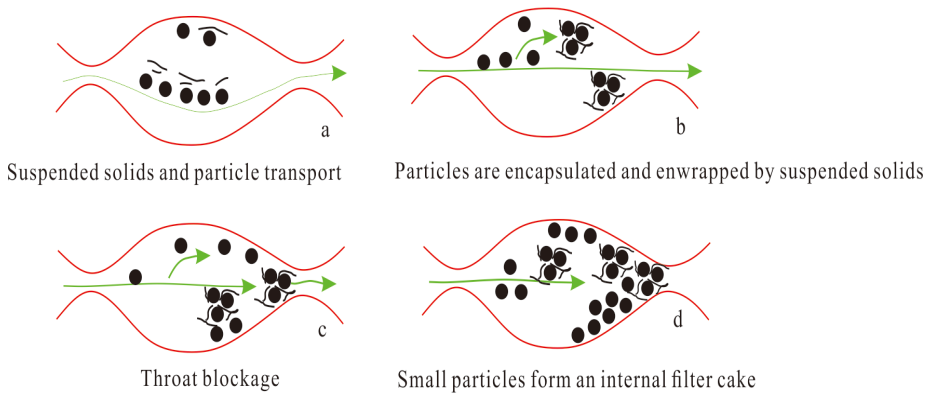

Figure 1. Microparticles and suspended solids migrate and block pore throats.

The suspended solids in the injected water are mainly composed of organic matter, including straight-chain hydrocarbons and colloidal asphaltenes, while inorganic substances are primarily composed of iron corrosion products, calcium scale, and formation minerals. During the water injection process, fine particles and suspended solids are transported together with the fluid. As fluid flows, fine particles and suspended solids are captured or deposited in the pore throats, gradually increasing resistance, narrowing fluid channels, and reducing permeability, as shown in Figure 1c.

A large number of suspended solids and clay mixed with fine particles can form a bridging structure in the pore throats, where the particles interact and bridge within the pores, gradually causing a filtration cake to form, as shown in Figure 1d. This ultimately blocks the pore throats and increases water injection pressure.

2.2. Fluids and Samples Preparation

In the core blockage due to fine particle migration, in addition to the impact of the core's own pore throats and permeability, it is primarily influenced by clay content and the size of the fine particles. This has been the focus of many related studies. Currently, attention is shifting to the location of fine particle migration blockages in the core and the resistance after blockage. Therefore, we varied the injection rates and conducted displacement experiments at 20 mL/min and 30 mL/min on cores with different permeability levels to determine the variation in injection pressure (or permeability) during the injection of water containing fine particles.

The injection water was prepared according to the ion analysis of water samples, with water quality details as shown in Table 1. The fine particles and suspended solids in the injection water are detailed in Table 2. In the experiment, 4000-mesh quartz powder (mean diameter approximately 3–5 μm) was used to simulate suspended solids in the injection water, as shown in Figure 2b, and #0 diesel was used to simulate oil content in the injection water.

Table 1. Ion analysis of injection water.

Water Sample	Ion Concentration mg/L								PH
Ion Types	K^+	Na^+	Ca^{2+}	Mg^{2+}	Fe^{2+}	Cl^-	$SO4^{2-}$	HCO^{3-}	
Injection Water	344	11×10^3	428	11×10^3	0.17	1.78×10^3	2.36×10^4	93.4	8.18

Table 2. Analysis of fine particles in injection water.

Injection Water	Suspended Solids mg/L	Median Particle Size d μm	Oil Content mg/L
Value	3–5	4	20

To test the migration and blockage location of fine particles and the resistance after blockage, we focus on the blockage conditions in both homogeneous and heterogeneous cores. The core is an artificial core with a total length of 1 m, divided into 4 sections, each 0.25 m long. Each section is equipped with two pressure gauges.

For homogeneous cores, prepare sufficient clay and gravel. The clay consists of illite and montmorillonite, making up 10% of the total, with the remainder being gravel with a mean particle size of 89 μm. According to the experimental plan, mix the clay and gravel evenly and load them into the core barrel. Measure the average permeability, ensuring that the pressure differentials between the five gauges (A, B, C, D, and E) remain constant. At this point, the core is considered to be homogeneous, with a permeability of 400 mD, as shown in Figure 3a.

Figure 2. (**a**) Experimental uartz sand; (**b**) Quartz powder.

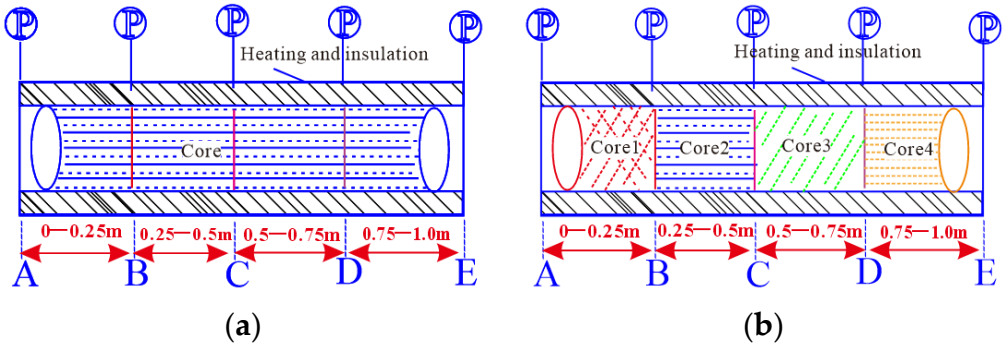

Figure 3. (**a**) Schematic diagram of homogeneous core; (**b**) Schematic diagram of heterogeneous core.

For heterogeneous cores, adjust the gravel quantity in the 4 sections, but ensure that the clay makes up 10% of the total in each section. Test the permeability in the core barrel to achieve target permeabilities of 200 mD, 400 mD, 800 mD, and 1000 mD for each section, respectively, by adjusting the amount of clay and gravel. Then, according to the required clay and gravel quantities for each section, divide the core into four segments and test the permeability. After testing, transfer the clay and gravel into another prepared core barrel. This method ensures that the four sections have permeabilities of 200 mD, 400 mD, 800 mD, and 1000 mD, respectively. The specific core segmentation is shown in Figure 3b.

2.3. Physical Experimental Simulation Methods for Blockage Location and Blockage Resistance Due to Fine Particles and Suspended Solids

The experiment was conducted using a self-developed multi-section composite core fluid permeability testing device, as shown in Figure 4. This setup was used to simulate the migration and blockage process of fine particles during water injection. The experiment aimed to observe the locations of fine particle blockages and the pressure after blockage. The core length was 1 m, with pressure gauges installed at intervals of 0.25 m, resulting in five gauges (A, B, C, D, and E) and dividing the core into four sections, as shown in Figure 4.

The test method allows for clear recording of pressure and permeability changes in each section, enabling the analysis of core blockage locations and the calculation of blockage pressure differentials.

The experimental steps are as follows:

The core used in the experiment was an artificial core composed of clay and gravel. The clay consisted of illite and montmorillonite, as shown in Figure 2a. The remaining material was gravel, with an average particle size of 89 μm.

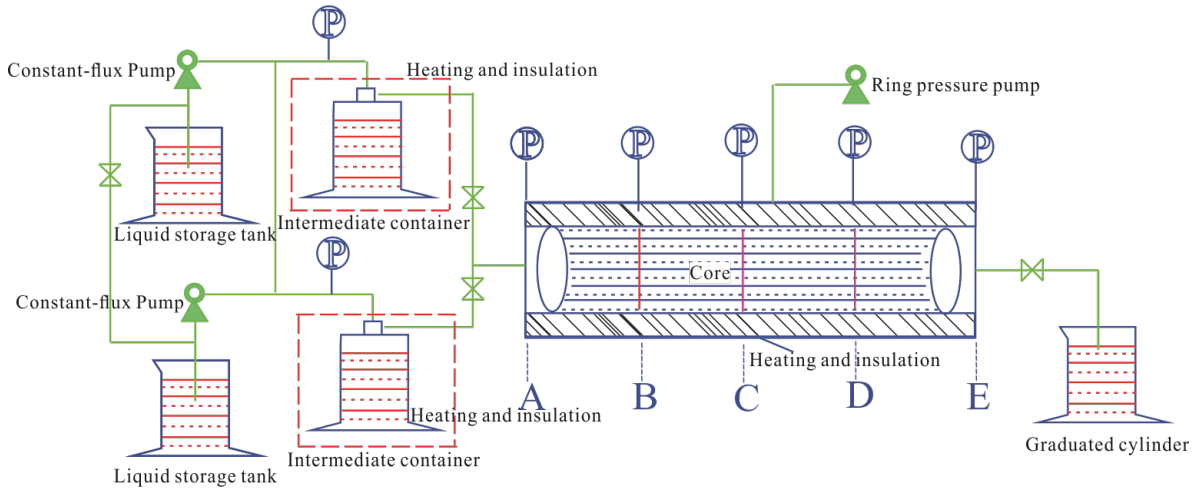

Figure 4. Schematic diagram of the experimental process.

The clay and gravel were mixed evenly and placed into the core barrel to form the artificial core, which was then installed in the core holder.

The experiment used an INSTE electromagnetic flowmeter, which has a measurement accuracy of ±0.1% to measure the air permeability of the experimental core, denoted as K_i.

We prepared working fluids under different water quality conditions, using a 4000-mesh quartz powder (mean diameter approximately 3–5 μm), as shown in Figure 5, to simulate suspended solids in the injected water.

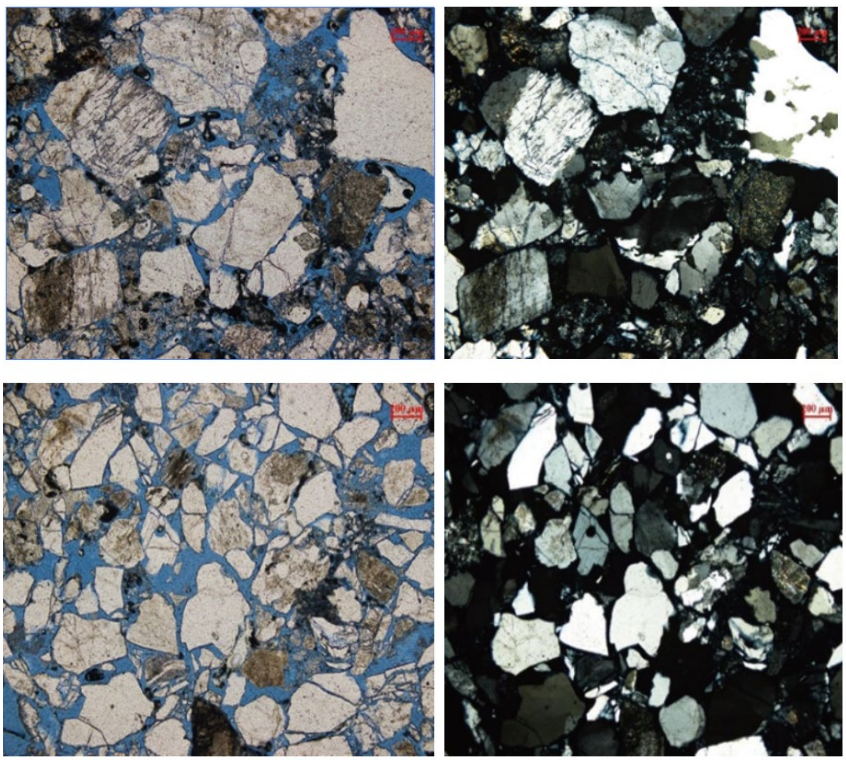

Figure 5. The microscopic morphology of interstitial components.

We maintained the formation temperature conditions and displaced a certain volume of working fluid at a constant flow rate. After the core permeability stabilized, we measured its permeability, denoted as K_j.

We recorded the pressure and permeability of each section (AB, BC, CD, and DE) under different constant flow rates.

We evaluated the impact of injected water blockage on the core's flow resistance according to the following permeability formula:

$$k_i = \frac{Q\mu L}{A\Delta p} \tag{1}$$

where k_i represents the last permeability, D; Q represents the injection rate, cm^3/s; μ represents the fluid viscosity, mPa.s; L represents the length, cm; and A represents the cross-sectional area of the core, cm^2.

The pressure differentials for sections AB, BC, CD, and DE are represented as follows:

$$\Delta p_{i,j} = p_j - p_i = \frac{Q\mu(L_j - L_i)}{Ak_j} \tag{2}$$

In the formula, $\Delta p_{i,j}$ represents the pressure differential for each section, 10^{-1} MPa; p_i, p_j represent the pressures at points i and j, where i and j correspond to the sections A, B; B, C; C, D; and D, E, respectively; k_j represents the permeability of each section, D; and L represents the length, L_i, L_j represent the pressures at points i and j, cm.

Given the pressure differentials for each section, the pressure for the entire segment during water injection is as follows:

$$p = Q(\frac{udx}{Ak_1} + \frac{udx}{Ak_2} + \cdots + \frac{udx}{Ak_n}) = Q\sum_{i=1}^{i=n} \frac{1}{k_j}\frac{udx}{A} \tag{3}$$

In the formula, dx represents the distance from entrance to the exit in cm.

2.4. Micromorphology Analysis of Blockages

Using the FEI Quanta250 SEM field emission scanning electron microscope, manufactured by FEI (Hillsboro, OR, USA) and sourced in the United States, with a strong association with Hillsboro, Oregon, we observed the blockage materials in the core during the experiment. The resolution of the secondary electron images reached 1.04 nm, with a magnification range of 15 to 300,000 times, allowing for casting thin sections analysis of the blockages [35]. The casting thin sections can identify interstitial components such as clay and silt particles. Casting thin section tests on oilfield reservoir rocks, as shown in Figure 5, reveal that the reservoir rocks are loosely cemented with argillaceous cement. The interstitial content is high and unevenly distributed. The reservoir lithology consists of medium- to coarse-grained feldspathic lithic sandstone and lithic feldspar sandstone. The clay-sized interstitial material has a particle size of less than 8 μm, accounting for 0.16% to 2.83%, with an average of 0.68%. The proportion of interstitial clay-sized material with particle sizes between 8 μm and 63 μm ranges from 6.36% to 40.48%, with an average of 11.98%.

The powder X-ray diffraction (XRD) analysis was conducted on dried blockage samples. The samples were separated using standard sieving and ground to a powder with a particle size of less than 2 μm for XRD analysis of the inorganic components. Based on the XRD spectra and comparison with standard diffraction patterns, the components of the inorganic blockages were identified.

The XRD spectrum of the blockage material from well B-Q-2 is shown in Figure 6. By comparing with standard diffraction patterns of minerals such as hematite (Fe_2O_3), it was determined that the blockage material may contain Fe_2O_3, $Al_4(OH)_8(Si_4O_{10})$, and $Zn_5(OH)_6(CO_3)_2$. The diffraction peaks match those of the standard patterns, with the highest match corresponding to hematite (Fe_2O_3). Peaks at 2θ of 24.149°, 33.161°, 35.629°, 40.862°, 49.463°, 54.073°, 62.436°, and 63.998° correspond to the (012), (104), (110), (113), (024), (116), (214), and (300) crystal planes of hematite.

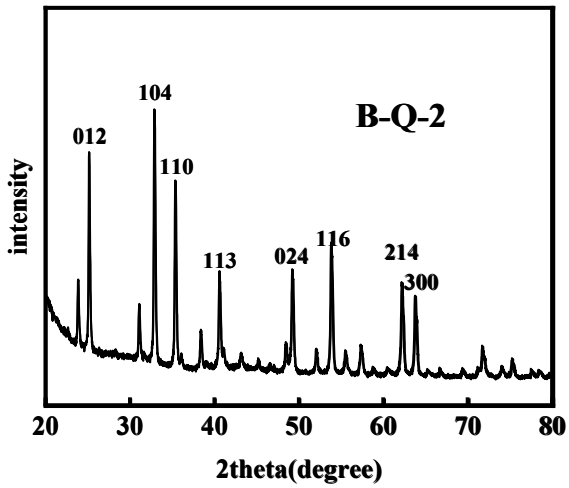

Figure 6. XRD analysis of the inorganic components in blockage materials.

Analysis of the blockage material composition indicates that the blockage in well B-Q-2 is primarily composed of hydrated silicates and alkali metal oxides. This suggests the presence of clay minerals and quartz sand in the blockage, likely due to formation sand production and wellbore collapse. Hematite is identified as a product of corrosion from formation minerals and downhole metal pipes.

In well B-Q-2, blockage primarily results from the migration of clay and fine rock particles. It can be inferred that under the influence of external fluids, particularly high-viscosity solutions, fine particle migration is likely to occur, with detached fine particles further promoting scale formation. Additionally, exposed rock particles can be observed in the dried and de-oiled blockage materials, which visually demonstrates that fine particles have been detached and mixed into the composite scale, with a large amount of inorganic particles encapsulated within the composite scale. From a microscopic perspective, it is evident that small particles are present in the scale.

Under the erosion of the solution fluid, loosely cemented fine particles undergo detachment and migration. On one hand, fine particles can act as nuclei for crystal formation, attracting oil molecules and forming precipitates. On the other hand, detached fine particles can entangle with inorganic salt crystals/oil, forming more complex composite scales with the fine particles, which leads to blockage.

3. Results and Discussion

To test the migration and blockage location of fine particles and the resistance after blockage, blockage simulations were conducted using both homogeneous and heterogeneous cores. The analysis focused on the blockage locations after fine particle migration and the calculation of blockage resistance. By comparing the blockages in homogeneous and heterogeneous cores, the study clearly determined that different core permeabilities result in different blockage locations and pressures due to fine particle migration.

3.1. Blockage Resistance of Homogeneous Core under Different Injection Flow Rates

In the testing system, an artificial core was installed, and the initial permeability of the artificial core was measured to be 396.17 mD. Displacement experiments were conducted at an injection rate of 20 mL/min, with a test duration of 180 min. The permeability and pressure for sections AB, BC, CD, and DE were analyzed, as shown in Figure 7a,b.

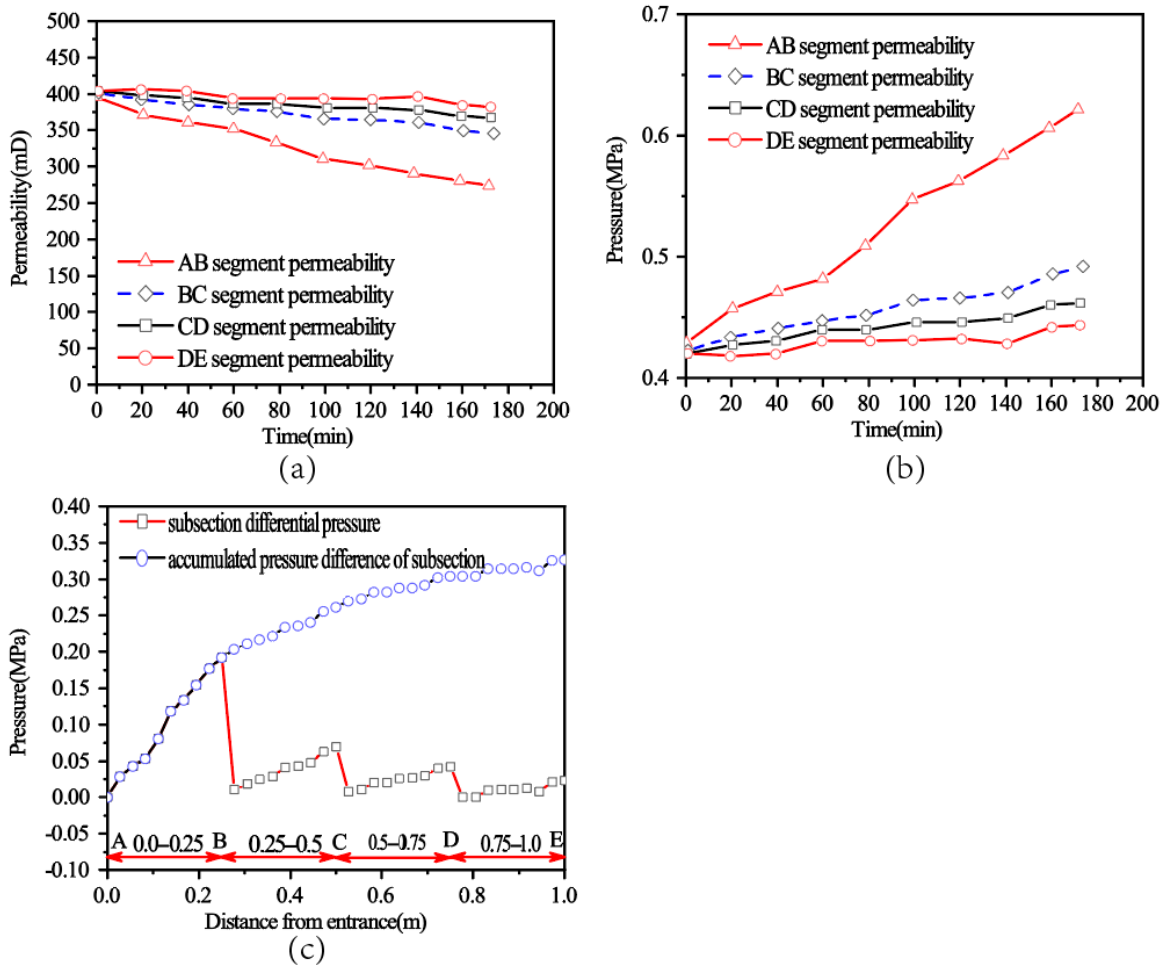

Figure 7. Homogeneous core at 20 mL/min: (**a**) reduction in permeability due to blockage, (**b**) increase in blockage pressure, and (**c**) overall net pressure after blockage.

Figure 7a shows that for the homogeneous core, with an initial permeability of 396.17 mD, as the injection time increases, blockage first occurs in the inlet section, AB. The permeability decreases accordingly, and after 180 min of injection, the permeability of the AB section drops to 171.79 mD, representing a 31.03% decrease. Similarly, the permeability decrease rates for the BC, CD, and DE sections are 14.07%, 9.10%, and 5.70%, respectively.

It is concluded that the initial blockage occurs at the injection inlet, and over time, fine particles and suspended solids migrate deeper into the core. Blockage then occurs in the BC section. However, in the BC section, since fine particles and suspended solids have already deposited at the inlet of the AB section, the amount of particles and solids migrating into the core decreases, leading to less blockage in the BC section compared to the AB section. Similarly, the blockage in the CD section is less severe than in the BC section, and the blockage in the DE section is less severe than in the CD section.

Figure 7b shows that for the homogeneous core, blockage at the initial injection inlet causes a significant increase in injection pressure. The injection pressure rises from 0.43 MPa to 0.62 MPa, representing a 45.00% increase. Similarly, the pressure increase rates for the BC, CD, and DE sections are 16.37%, 10.02%, and 6.05%, respectively. Fine particles and suspended solids primarily deposit at the inlet, causing the injection pressure to increase.

The increase in pressure is inversely related to permeability. Greater decreases in permeability correspond to larger increases in pressure.

To determine the net pressure caused by blockage during the injection process, net pressure calculations were performed for sections AB, BC, CD, and DE, which are the pressures at the final time minus the pressures at the initial time. The net pressures for

each section were then summed sequentially, as shown in Figure 7c. At an injection rate of 20 mL/min, after 180 min of injection, the maximum net injection pressure reached 0.33 MPa. The net pressure of each section shows an exponential distribution, indicating that injection resistance tends to stabilize over time and with increasing core length, with slow increases. The net pressure increase rates for sections AB, BC, CD, and DE gradually decrease and approach a parallel straight line. The analysis suggests that at higher flow rates, significant microparticle migration occurred in the first section. Due to the large displacement pressure differential, these microparticles sequentially entered the subsequent sections, resulting in formation plugging and reduced permeability.

In the testing system, an artificial core was installed, and the initial permeability of the artificial core was measured to be 396.55 mD. Displacement experiments were conducted at an injection rate of 30 mL/min, with a test duration of 180 min. The permeability and pressure for sections AB, BC, CD, and DE were analyzed, as shown in Figure 8a,b.

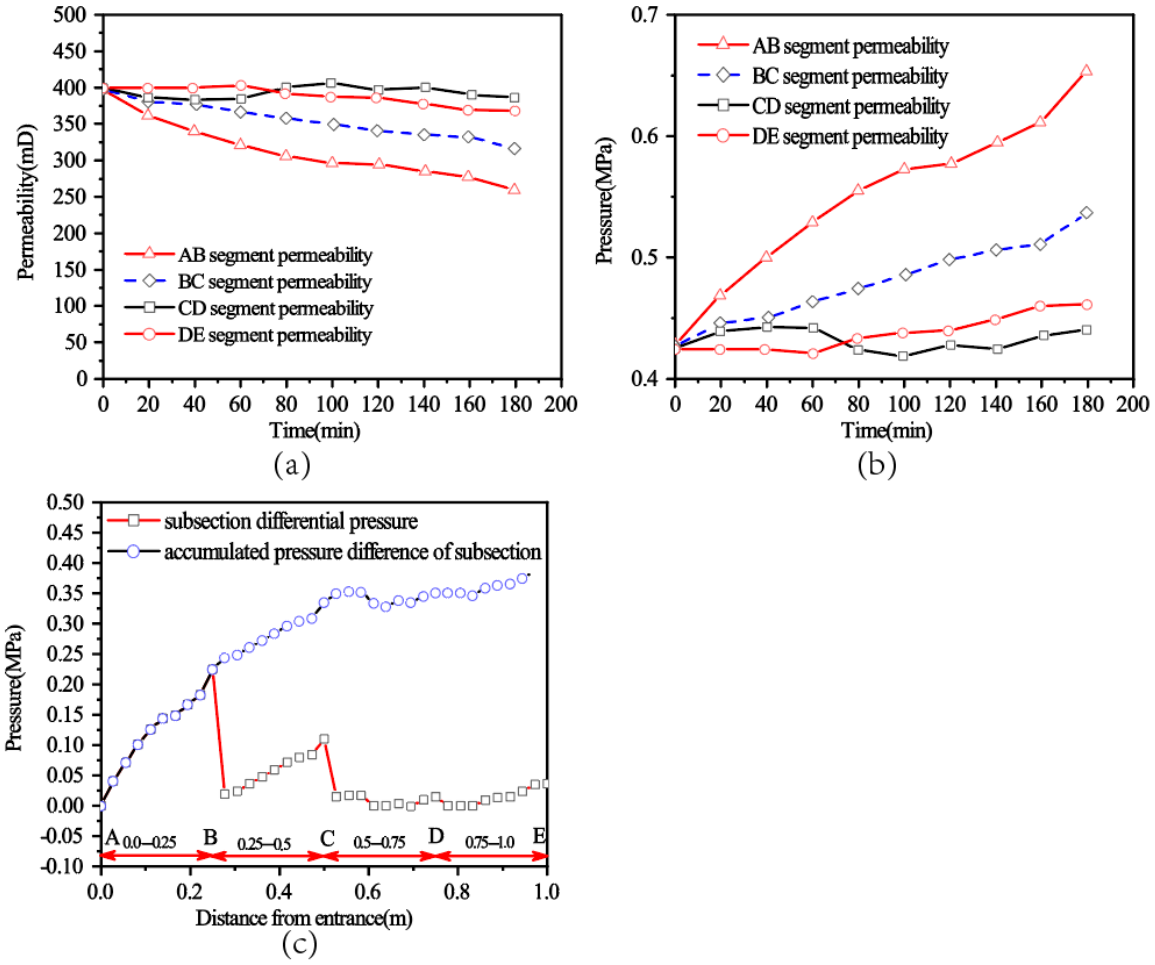

Figure 8. Homogeneous core at 30 mL/min: (**a**) reduction in permeability due to blockage, (**b**) increase in blockage pressure, and (**c**) overall net pressure after blockage.

Figure 8a shows that for the homogeneous core, with an initial permeability of 396.55 mD, blockage first occurs in the inlet section, AB, as the injection time increases. The permeability decreases accordingly, and after 180 min of injection, the permeability of the AB section drops to 259.92 mD, representing a 34.46% decrease. Similarly, the permeability decrease rates for the BC, CD, and DE sections are 20.54%, 5.41%, and 8.82%, respectively.

It is concluded that the initial blockage occurs at the injection inlet. As time progresses, fine particles and suspended solids in the injection water migrate deeper into the core, leading to blockage in the BC section. However, in the BC section, since fine particles

and suspended solids have already deposited at the inlet of the AB section, the number of particles and solids migrating deeper into the core decreases, resulting in less blockage in the BC section compared to the AB section. Similarly, the blockage in the CD section is less severe than in the BC section, and the blockage in the DE section is less severe than in the CD section.

Figure 8b shows that for the homogeneous core, blockage at the initial injection inlet causes a significant increase in injection pressure. The injection pressure rises from 0.42 MPa to 0.65 MPa, representing a 52.57% increase. Similarly, the pressure increase rates for the BC, CD, and DE sections are 25.85%, 5.72%, and 9.67%, respectively. Fine particles and suspended solids primarily deposit at the inlet, causing the injection pressure to increase.

The increase in pressure is inversely related to permeability. Greater decreases in permeability correspond to larger increases in pressure.

To determine the net pressure caused by blockage during the injection process, net pressure calculations were performed for sections AB, BC, CD, and DE, which are the pressures at the final time minus the pressures at the initial time. The net pressures for each section were then summed sequentially, as shown in Figure 8c. At an injection rate of 30 mL/min, after 180 min of injection, the maximum net injection pressure reached 0.36 MPa. The net pressure for each section shows an exponential distribution, indicating that injection resistance tends to stabilize over time and with increasing core length, with slow increases. The net pressure increase rates for sections AB, BC, CD, and DE gradually decrease and approach a parallel straight line. It indicates that as the displacement velocity increases, skeleton damage occurs near the wellbore, leading to more movable microparticles in the formation. High flow rates and high concentrations of movable sand cause the migration and plugging of microparticles over a greater range, resulting in a larger decrease in formation permeability and a greater increase in net pressure.

For the homogeneous core with constant permeability, comparing the blocking resistance of the core under two different injection rates (20 mL/min and 30 mL/min), it is observed that the blocking resistance is slightly higher at the 30 mL/min injection rate compared to the 20 mL/min rate. The net pressure increase values and trends are generally consistent, showing an exponential change. Additionally, the trend of blocking resistance changes for each section is similar, as shown in Figure 9.

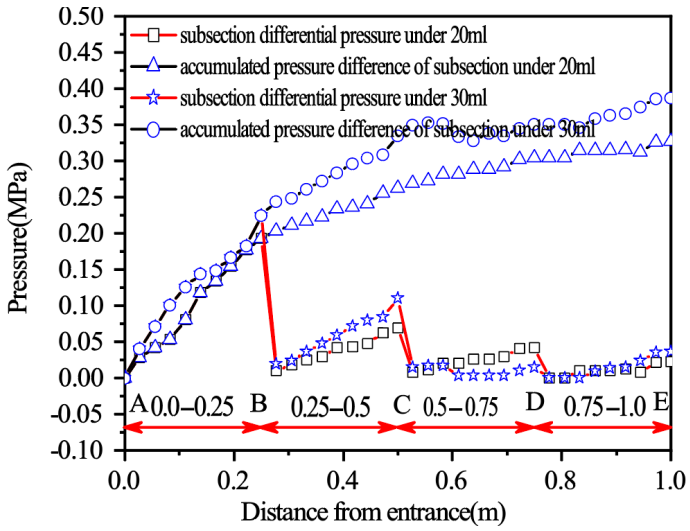

Figure 9. Comparison of core blocking resistance under injection rates of 20 mL/min and 30 mL/min.

In both cases, the blockage position is essentially the same, occurring primarily at the initial injection segment. This indicates that the blockage mechanism is fundamentally similar.

3.2. Resistance Analysis of Heterogeneous Core Plugging

For heterogeneous cores, each 0.25 m is divided into a segment, resulting in a total of four segments: AB, BC, CD, and DE from inlet to outlet. To simulate variations in permeability due to heterogeneity, artificial cores were prepared with the following permeabilities: AB segment 200 mD, BC segment 400 mD, CD segment 800 mD, and DE segment 1000 mD. The actual permeabilities were AB segment 195 mD, BC segment 397 mD, CD segment 812 mD, and DE segment 1030 mD. The permeability of each segment is shown in Table 3.

Table 3. Segmented permeability.

Non-Homogeneous Core Segments	Segment AB	Segment BC	Segment CD	Segment DE
Permeability/mD	195	397	812	1030

Figure 10a shows that for the heterogeneous core, the initial permeability of the inlet segment is 195 mD. Significant blockage occurs at the inlet, with the permeability of the AB segment reducing to 92.68 mD after 180 min of injection. The permeability reduction rate reaches 53.14%, which is notably higher than the reduction rate observed in homogeneous cores with an initial permeability of 400 mD. This indicates that cores with lower permeability are more prone to blockage.

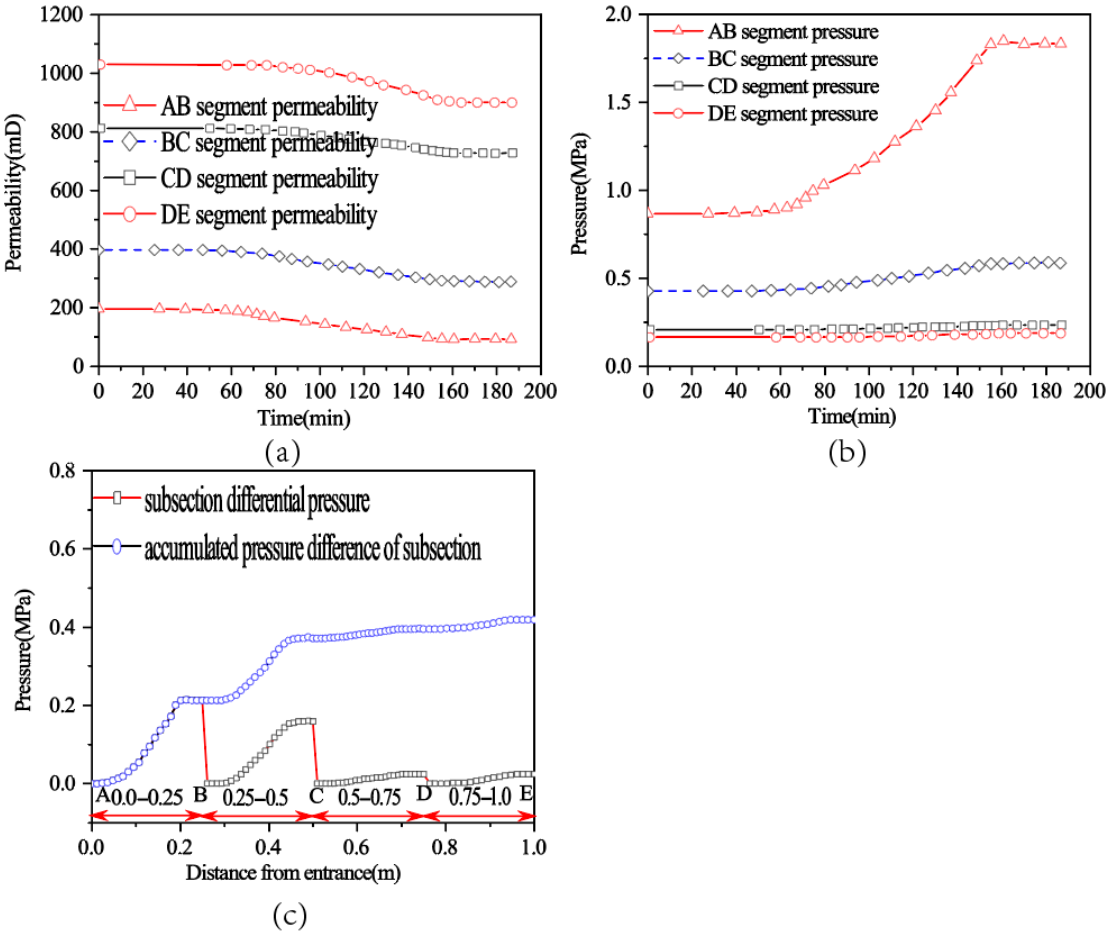

Figure 10. Non-homogeneous core under 30 mL/min conditions: (**a**) permeability of each core segment, (**b**) pressure of each core segment, (**c**) comparison of net pressure for the entire core and segmental pressures.

Similarly, the permeability reduction rate for the BC segment reaches 27.40%, also higher than in homogeneous cores with an initial permeability of 400 mD. The reduction rates for the CD and DE segments are 10.45% and 12.58%, respectively, slightly higher than those in homogeneous cores.

Figure 10b shows that for the heterogeneous core, significant increases in injection pressure are observed due to blockage at the inlet. The injection pressure rises from 0.87 MPa to 1.83 MPa, with an increase rate of 113.4%, which is significantly higher than in homogeneous cores.

Similarly, the pressure increase rates for the BC, CD, and DE segments are 37.74%, 11.66%, and 14.38%, respectively, all higher than the increase rates in homogeneous cores with an initial permeability of 400 mD.

To determine the net pressure caused by blockage during the injection process, net pressure was calculated for each segment (AB, BC, CD, and DE) by subtracting the initial pressure from the final pressure for each segment. The net pressures for each segment were then summed up, as shown in Figure 10c. For the 30 mL/min injection rate, the maximum net pressure reaches 0.42 MPa after 180 min of injection, which is higher than in homogeneous cores. The net pressures for the AB and BC segments increase linearly, while the increase slopes for the CD and DE segments gradually decrease, approaching a parallel line. This indicates that in heterogeneous conditions, blockage is more severe, with a longer blockage length compared to homogeneous cores, with blockage length being twice that of homogeneous cores.

Adjusting non-homogeneous core positions. The non-homogeneous core was created with the following properties: AB segment with 1000 mD, BC segment with 800 mD, CD segment with 400 mD, and DE segment with 200 mD. Actual values are as follows: AB segment 1050 mD, BC segment 796 mD, CD segment 410 mD, and DE segment 210 mD. Permeability values for each segment are shown in Table 4.

Table 4. Segmented permeability.

Non-Homogeneous Core Segments	Segment AB	Segment BC	Segment CD	Segment DE
Permeability/mD	1050	796	410	210

Figure 11a For the non-homogeneous core, the initial permeability of the AB segment was 1050 mD, with no significant blockage observed. After 180 min of injection, the permeability of the AB segment decreased to 942.66 mD, a reduction rate of 10.22%. However, the permeability reduction rate for the BC segment was 40.85%, which is significantly higher than that of the homogeneous core with an initial permeability of 400 mD. This indicates that non-homogeneous cores are more prone to blockage. Permeability reduction rates for the CD and DE segments were 4.40% and 2.79%, respectively, similar to the homogeneous core case.

Figure 11b For the non-homogeneous core, blockage occurred at the BC segment, leading to a significant increase in injection pressure. The injection pressure rose from 0.21 MPa to 0.72 MPa, with a pressure increase rate of 250.73%. This is noticeably higher than in the homogeneous core.

Similarly, pressure increase rates for the CD and DE segments were 4.60% and 2.87%, respectively, similar to the homogeneous core situation.

Figure 11c To determine the net pressure caused by blockage during the injection process, the net pressure for each segment (AB, BC, CD, DE) was calculated by subtracting the initial pressure from the final pressure for each segment. Net pressures were then summed, as shown in Figure 10c. With a 30 mL/min injection rate over 180 min, the maximum net injection pressure reached 0.34 MPa. This is consistent with the homogeneous core situation but lower than the low-permeability AB segment case. The net pressure for the BC segment increased linearly, while the net pressures for the CD and DE segments

approached a parallel line. This indicates that in non-homogeneous conditions, the length of blockage is twice that of the homogeneous core.

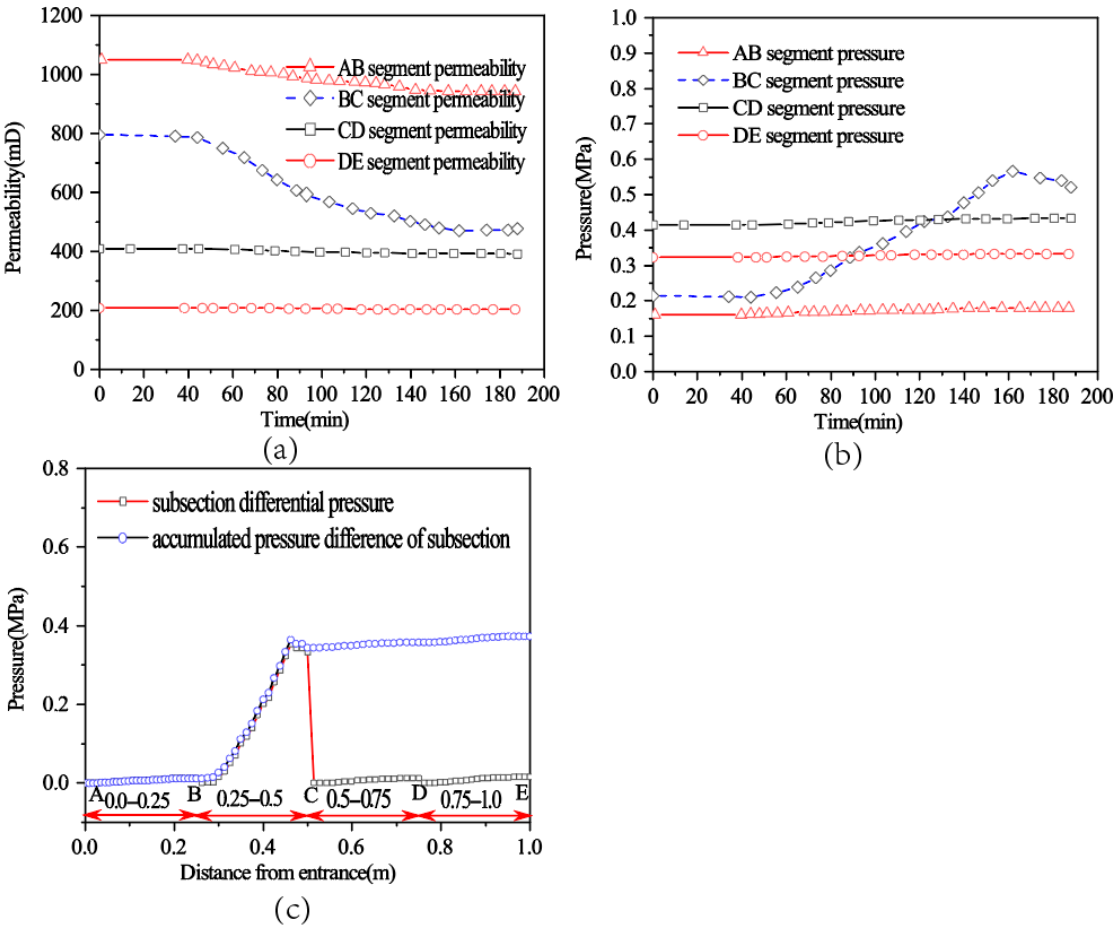

Figure 11. Non-homogeneous core under 30 mL/min conditions: (**a**) permeability of each core segment, (**b**) pressure of each core segment, (**c**) comparison of net pressure for the entire core and segmental pressures.

Compared to homogeneous cores, non-homogeneous cores with varying permeability from low to high and from high to low are analyzed in three scenarios. In the scenario where permeability increases from low to high, the initial permeability of the entrance segment is 195 mD, resulting in severe blockage. The injection pressure for blockage is higher than that for both homogeneous cores and non-homogeneous cores, with permeability decreasing from high to low, as shown in Figure 12.

For both homogeneous cores and non-homogeneous cores where permeability decreases from high to low, the blockage location in the non-homogeneous core is twice that of the homogeneous core, though the final blockage pressure is similar in both cases. This indicates that if the initial permeability at the entrance is lower than that of other segments, significant blockage will occur, leading to higher blockage resistance. Conversely, if the initial permeability at the entrance is higher than that of other segments, blockage will occur but will have a smaller impact on blockage resistance. The final blockage resistance in this scenario will be close to that of the homogeneous core.

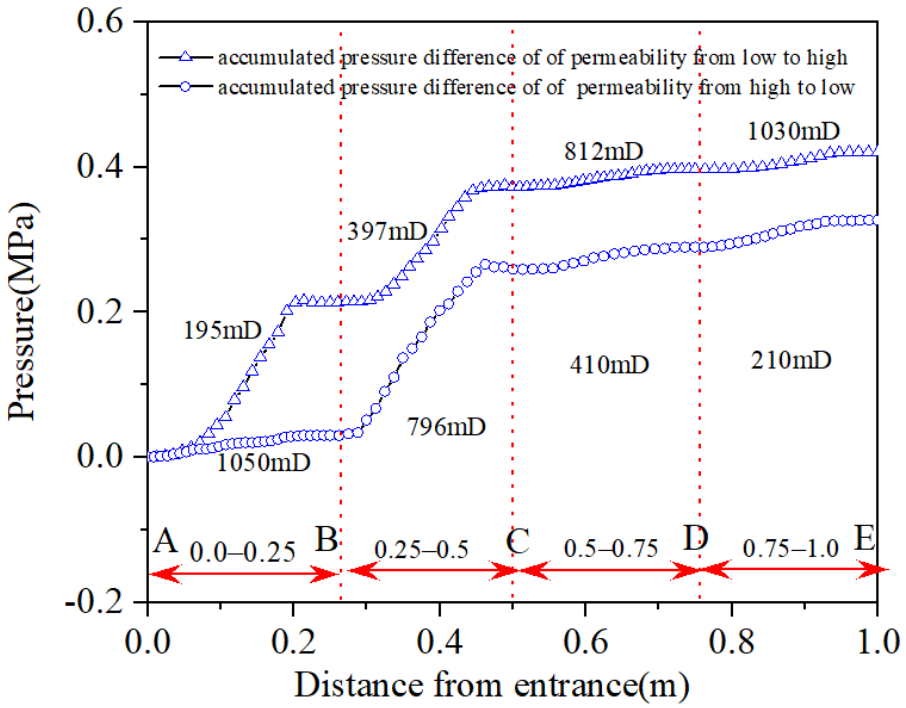

Figure 12. Comparison of blockage resistance in homogeneous cores and non-homogeneous cores under two scenarios: permeability increasing from low to high and permeability decreasing from high to low.

4. Conclusions

In this paper, the experiments were conducted to simulate reservoirs with different permeabilities in parallel, monitoring parameters such as the displacement flow rate and permeability changes in the parallel cores. The study evaluated the impact of inter-layer heterogeneity on water injection capacity and clarified how permeability variations and injection flow rates affect blockage location and resistance.

The research found that the blockage location and length in non-homogeneous cores were twice those in homogeneous cores. When the initial permeability at the entrance is lower than that of other sections, it results in higher blockage resistance. Conversely, when the initial permeability at the entrance is higher than in other sections, the impact on blockage resistance is smaller, and the final blockage resistance is similar to that in homogeneous cores. Specifically, the final resistance caused by a lower initial permeability at the entrance is 1.27 times greater than the blockage resistance observed in homogeneous cores.

Compared to homogeneous cores, heterogeneous cores experience more severe blockage in the near-well zone. Experimental results show that it requires twice the unplugging pressure to address the blockage pressure in the near-well zone.

This study only investigated blockage experiments under a single water quality and particle type. The research conditions are quite limited. To gain a comprehensive understanding of core blockage mechanisms under water injection, it is recommended to vary the water quality and particle sizes and conduct experiments on core blockage under both homogeneous and non-homogeneous conditions to further analyze blockage pressures. Additionally, developing models for the plugging position and plugging pressure in water injection wells and combining theoretical models with experiments can further guide practical production and solve the problem of injection difficulties caused by plugging in water injection wells.

Author Contributions: Conceptualization, methodology, validation, investigation, data curation, writing—original draft preparation, and writing—review and editing, H.C. and M.W.; validation, visualization, and supervision, J.Y., T.H. and X.Z. (Xiaotong Zhang); investigation, supervision,

and project administration, Y.C. and J.P.; project administration, validation, and formal analysis, X.Z. (Xiaopeng Zhai) and W.Z.; review and editing, resources, funding acquisition, H.C. and X.Z. (Xiaopeng Zhai). All authors have read and agreed to the published version of the manuscript.

Funding: This research was funded by the Open Fund Project of the National Key Laboratory of Efficient Development of Offshore Oil and Gas (No. CCL2023RCPS0168RQN).

Data Availability Statement: The data presented in this study are available upon request from the corresponding authors.

Acknowledgments: We thank the Open Fund Project of the National Key Laboratory of Efficient Development of Offshore Oil and Gas for its support with analysis and testing. We also thank the Hubei Key Laboratory of Oil and Gas Drilling and Production Engineering for its support with analysis and testing.

Conflicts of Interest: Author Jifei Yu, Huan Chen, Yanfeng Cao, Min Wen, Xiaotong Zhang, Tongchuan Hao, Jianlin Peng and Weitao Zhu were employed by the company CNOOC Research Institute Co., Ltd. The remaining authors declare that the research was conducted in the absence of any commercial or financial relationships that could be construed as a potential conflict of interest.

References

1. Qu, Z.; Li, Y.; Wang, L. Quantitative characterization methods of plugging position of offshore polymer flooding reservoir. *Fault-Block Oil Gas Field* **2019**, *26*, 360–363.
2. Ding, Y.; Zhao, Y.; Wen, X.; Liu, Y.; Feng, M.; Rui, Z. Development and Applications of CO2-Responsive Gels in CO2 Flooding and Geological Storage. *Gels* **2023**, *9*, 936. [CrossRef] [PubMed]
3. Yao, Z.; Zhao, Y.; Li, J.; Luo, T.; Yang, H. Study on the change law of physical properties after water flooding. *Unconv. Oil Gas* **2021**, *8*, 45–61.
4. Shaowei, W.; Hongyu, Z.; Kexiong, L. An integrated working fluid for blocking removal and sand control in offshore wells blocked by particle migration. *Drill. Fluid Complet. Fluid* **2021**, *38*, 391–396.
5. Yang, R.; Zhang, J.; Chen, H.; Jiang, R.; Sun, Z.; Rui, Z. The injectivity variation prediction model for water flooding oilfields sustainable development. *Energy* **2019**, *189*, 116317. [CrossRef]
6. Cai, J.; Chen, X.; Wu, D.; Chen, B.; Pan, Y. A New Method to Predict Water Breakthrough in Intelligent Completion Horizontal Well. *Energy Fuels* **2023**, *37*, 17438–17451. [CrossRef]
7. Zhang, H.; He, S.; Jiao, C.; Luan, G.; Mo, S.; Lei, G. Investigation of dynamic effect of capillary pressure in ultra-low permeability sandstones. *Indian Geotech. J.* **2015**, *45*, 79−88. [CrossRef]
8. Jia, K.; Zeng, J.; Wang, X.; Li, B.; Gao, X.; Wang, K. Wettability of tight sandstone reservoir and its impacts on the oil migration and accumulation: A case study of Shahejie formation in Dongying depression, Bohai Bay Basin. *Energies* **2022**, *15*, 4267. [CrossRef]
9. Mirzaei, M.; Das, D.B. Dynamic effects in capillary pressure saturations relationships for two-phase flow in 3D porous media: Implications of micro-heterogeneities. *Chem. Eng. Sci.* **2007**, *62*, 1927−1947. [CrossRef]
10. Manthey, S.; Hassanizadeh, S.M.; Helmig, R.; Hilfer, R. Dimensional analysis of two-phase flow including a rate-dependent capillary pressur saturation relationship. *Adv. Water Resour.* **2008**, *31*, 1137−1150. [CrossRef]
11. Sa, J.H.; Sum, A.K. Promoting gas hydrate formation with ice-nucleating additives for hydrate-based applications. *Appl. Energy* **2019**, *251*, 113352. [CrossRef]
12. Sui, Y.; Cao, G.; Guo, T.; Li, Z.; Bai, Y.; Li, D.; Zhang, Z. Development of gelled acid system in high-temperature carbonate reservoirs. *J. Pet. Sci. Eng.* **2022**, *216*, 110836. [CrossRef]
13. Nguyen, N.N.; Nguyen, A.V.; Nguyen, K.T.; Rintoul, L.; Dang, L.X. Unexpected inhibition of CO2 gas hydrate formation in dilute TBAB solutions and the critical role of interfacial water structure. *Fuel* **2016**, *185*, 517–523. [CrossRef]
14. Sun, J.; Sun, L.; Liu, W. Alkaline consumption mechanisms by crude oil: A comparison of sodium carbonate and sodium hydroxide. *Colloids Surf. A Physicochem. Eng. Asp.* **2008**, *315*, 38–43. [CrossRef]
15. Li, H.; Wang, X.; Ma, C.; Lu, Y.; Han, S.; Chen, C.; Zhang, J. Effect of electrical treatment on structural behaviors of gelled waxy crude oil. *Fuel* **2019**, *253*, 647–661. [CrossRef]
16. Starr, F.W.; Schroder, T.B.; Glotzer, S.C. Molecular dynamics simulation of a polymer melt with a nanoscopic particle. *Macromolecules* **2002**, *35*, 4481–4492. [CrossRef]
17. Avella, M.; Cosco, S.; Di Lorenzo, M.; Di Pace, E.; Errico, M. Influence of CaCO3 nanoparticles shape on thermal and crystallization behavior of isotactic polypropylene based nanocomposites. *Therm. Anal. Calorim.* **2005**, *80*, 131–136. [CrossRef]
18. Wang, Y.; Chen, Z.; Wu, Z.J.; Li, Y.; Yang, W.; Li, Y.F. High-Efficiency production of graphene by supercritical CO2 exfoliation with rapid expansion. *Langmuir* **2018**, *34*, 7797–7804. [CrossRef]
19. Liu, Z.; Shi, B.; Ge, T.; Sui, F.; Wang, Y.; Zhang, P.; Chang, X.; Liu, Y.; Wang, Y.; Wang, Z. Tight sandstone reservoir sensitivity and damage mechanism analysis: A case study from Ordos Basin, China and implications for reservoir damage prevention. *Energy Geosci.* **2022**, *3*, 394–416. [CrossRef]

20. Mitra, A.; Harpalani, S.; Liu, S. Laboratory measurement and modeling of coal permeability with continued methane production: Part 1—Laboratory results. *Fuel* **2012**, *94*, 110–116. [CrossRef]
21. Yang, Y.; Li, Z.; Ji, H.; Peng, Y.; Liu, Z. Effect of soluble organic matter in coal on its pore structure and methane sorption characteristics. *J. Fuel Chem. Technol.* **2013**, *41*, 385–390.
22. Liu, Y.; She, Y.; Zhang, F.; Feng, Q.; Li, X.; Dong, H.; Sun, S. Mechanism of Nano-depressurization and Injection-Augmenting Technology and Its Application in China's Oilfields: Recent Advances and Perspectives. *Energy Fuels* **2022**, *36*, 10751–10765. [CrossRef]
23. Yao, B.; Li, C.; Yang, F.; Zhang, Y.; Xiao, Z.; Sun, G. Structural properties of gelled Changqing waxy crude oil benefitted with nanocomposite pour point depressant. *Fuel* **2016**, *184*, 544–554. [CrossRef]
24. Yang, H.; Wang, W.; Tian, Z. Reservoir damage mechanism and protection measures for coal bed methane. *J. China Coal Soc.* **2014**, *39*, 158–163.
25. Cheraghian, G.; Khalili Nezhad, S.S.; Kamari, M.; Hemmati, M.; Masihi, M.; Bazgir, S. Adsorption polymer on reservoir rock and role of the nanoparticles, clay and SiO2. *Int. Nano Lett.* **2014**, *4*, 114. [CrossRef]
26. Massarotto, P.; Iyer, R.S.; Elma, M.; Nicholson, T. An experimental study on characterizing coal bed methane (CBM) fines production and migration of mineral matter in coal beds. *Energy Fuels* **2014**, *28*, 766–773. [CrossRef]
27. Awan, F.U.R.; Keshavarz, A.; Akhondzadeh, H.; Nosrati, A.; Al-Anssari, S.; Iglauer, S. Optimizing the dispersion of coal fines using sodium dodecyl benzene sulfonate. In Proceedings of the Asia Pacific Unconventional Resources Technology Conference, Brisbane, Australia, 18–19 November 2019. URTEC-198250-MS.
28. Bai, T.; Chen, Z.; Aminossadati, S.M. Experimental investigation on the impact of coal fines generation and migration on coal permeability. *J. Pet. Sci. Eng.* **2017**, *159*, 257–266. [CrossRef]
29. Zeinijahromi, A.; Vaz, A.; Bedrikovetsky, P. Productivity impairment of gas wells due to fines migration. In Proceedings of the SPE International Symposium and Exhibition on Formation Damage Control, Lafayette, LA, USA, 15–17 February 2012. SPE 151774.
30. Prempeh, K.; Chequer, L.; Badalyan, A.; Bedrikovetsky, P. Effects of kaolinite on fines migration and formation damage. In Proceedings of the SPE International Conference and Exhibition on Formation Damage Control, Lafayette, LA, USA, 19–21 February 2020. SPE-199293-MS.
31. Wei, G.; Di, Q.F. Seepage model and experiments of drag reduction by nanoparticle adsorption. *J. Hydrodyn.* **2013**, *25*, 871–876.
32. Ma, C.; Zhang, J.; Feng, K.; Li, Z.; Chen, C.; Huang, Q.; Lu, Y. Influence of asphaltenes on the performance of electrical treatment of waxy oil. *J. Pet. Sci. Eng.* **2019**, *180*, 31–40. [CrossRef]
33. Moghadasi, J.; Müller-Steinhagen, H.; Jamialahmadi, M.; Sharif, A. Theoretical and experimental study of particle movement and deposition in porous media during water injection. *J. Pet. Sci. Eng.* **2004**, *43*, 163–181. [CrossRef]
34. EI-Amin, M.F.; Salama, A.; Sun, S. Numerical and dimensional analysis of nanoparticles transport with two-phase flow in porous media. *J. Pet. Sci. Eng.* **2015**, *128*, 53–64. [CrossRef]
35. Singh, S.B.; De, M. Thermally exfoliated graphene oxide for hydrogen storage. *Mater. Chem. Phys.* **2020**, *239*, 122102. [CrossRef]